View Article Online
DOI: 10.1039/C8NR06429F

2D Boron Nitride Nanosheets (BNNS) prepared by High-Pressure Homogenisation: Structure and Morphology

Valentina Guerra[1], Chaoying Wan[1], Volkan Degirmenci[2], Jeremy Sloan[3], Dimitris Presvytis[4], Tony McNally[1]*

[1]*International Institute for Nanocomposite Manufacturing (IINM), WMG,* [2]*School of Engineering and,* [3]*Department of Physics, University of Warwick, CV4 7AL, UK*

[4]*Thomas Swan & Co. Ltd, Consett, County Durham, DH87ND, UK*

E-mail: t.mcnally@warwick.ac.uk

Abstract

2D Boron Nitride Nano-sheets (BNNS) were prepared using a high-pressure homogenisation process to exfoliate bulk hexagonal boron nitride (h-BN). The effectiveness of this process was studied by characterising bulk h-BN and BNNS post-processing using numerous techniques. The BNNS produced was composed of a mixture of sheets having lengths on the nanometre (nm) scale, but lateral thicknesses on the micron (μm) length scale. The product was a macro-porous material containing slit-like pores with a surface area of 170 m^2/g. It had a polycrystalline structure with d_{002}=0.335 nm and L_{002}=2 nm. From the sharp E_{2g} peak in the Raman spectrum at 1360 cm^{-1} (FWHM = 12.5 cm^{-1}), the sheets had a low defect density and were highly exfoliated. X-Ray photoelectron spectroscopy (XPS) studies detected B-OH and N-H groups on the BNNS surface and the presence of residual surfactant. Contact angle measurements (60° ±3° (0 s); 40°± 2° (10 s)) confirmed a hydrophilic surface. The BNNS was thermally stable under oxidative conditions up to 323 °C.

View Article Online
DOI: 10.1039/C8NR06429F

1. Introduction

The combination of high performance chemical, physical and mechanical properties make nanomaterials very attractive for a range of industrial applications. Nanomaterials have at least one dimension on the nanometre (nm) scale and the uniqueness of many of their properties are due to a high surface-to-volume ratio and chemical structure on the nanoscale. 2D boron nitride nanosheets (BNNS) are increasingly of interest due to their relatively high thermal conductivity (300-360 W/mK (experimental)), structural stability and mechanical properties (elastic modulus: 220-510 Nm^{-1} (thickness about 1-2 nm)) [1, 2]. BNNS are composed of boron (B) and nitrogen (N) atoms with a B:N ratio of 1:1 and are isoelectronic with 2D graphene nanoplatelets (GNP). However, the aromatic structure of GNP makes them electrically conductive, while the partial ionic B-N=B bond confers electrical insulating characteristics to BNNS with a band gap of *ca.* 5.5 eV [1, 3, 4].

BNNS were first obtained in 2004 by exfoliating the bulk material (i.e. hexagonal boron nitride, h-BN), which is synthetically prepared since it is not present in nature [5]. Recently, different procedures have been adopted to obtain BNNS, such as ball milling [6], chemical exfoliation (sonication) [7-9], wet chemical reaction [3, 10], chemical vapour deposition (CVD) [11-14] and electron irradiation [15, 16].

One of the main applications of BNNS is as a functional additive for polymers where thermal management is required. Indeed, polymers are thermal insulators and the addition of BNNS may overcome this problem by transferring the external impulse from the polymer to the filler particles. For this purpose, a percolated network of BNNS is required, where the BNNS should be well dispersed and distributed throughout the polymer matrix. However, it is not easy to obtain a 3D interconnected BNNS structure in polymer matrices due to poor physical and chemical compatibility with polymers. Large interfaces are realised when BNNS is added to polymers, resulting in phonon scattering and poor thermal conduction [17-19].

View Article Online
DOI: 10.1039/C8NR06429F

Different strategies have been adopted to make BNNS compatible with polymer chains, including; surface modification [20-24], inclusion of functional particles [25] and, varying processing parameters (i.e. mixing capability, composition, alignment of filler particles) [26-29]. It is not possible to obtain composites with desired properties if the quality of the starting functional additive is not fit for purpose.

In this paper, we report, for the first time, the characterisation and properties of BNNS prepared using a proprietary large-scale procedure developed by Thomas Swan Ltd based on high-pressure homogenisation. The physicochemical properties of BNNS was examined thoroughly by surface characterization, morphology determination, crystallographic and thermal analysis, which are essential to reveal nanostructure and material properties. A laboratory scale (0.5g) high-pressure homogenisation process was used recently to prepare BNNS [30].

2. Experimental Methods

2.1 Preparation via high pressure homogenisation

BNNS were prepared using high-pressure homogenisation of bulk h-BN (hexagonal Boron Nitride). This proprietary process is based on the application of high shear forces achieved using a commercially available high-pressure homogeniser [31]. The bulk layered material, e.g. graphite or boron nitride, was mixed with a carrier liquid and other additives and subsequently introduced into the high-pressure homogeniser. The carrier liquid can be water or organic solvent and the additives can be surfactants or other materials as required by the application of interest. The mixture was processed in the high-pressure homogeniser, with the feed materials stored and supplied under ambient external conditions. By varying the processing conditions, in particular the operating pressure in the range 100 to1500 bar,

View Article Online
DOI: 10.1039/C8NR06429F

different degrees of exfoliation of the feed material can be achieved, thereby modifying the morphology and hence the properties of the platelets/sheets.

2.2 BNNS characterization

The BNNS produced was characterized using a range of techniques. Scanning Electron Microscopy (SEM) and Transmission Electron Microscopy (TEM) were used to examine the morphology and crystalline structure of BNNS along with X-ray Diffraction (XRD) and Raman spectroscopy. The surface properties were analysed by X-ray Photoelectron Spectroscopy (XPS), sessile tests and nitrogen physisorption. In addition, thermo-gravimetric analysis (TGA) was used to assess the thermal stability of the BNNS product.

SEM imaging was carried out using a Zeiss sigma field emission instrument, provided with a Gemini column. The images were recorded using the InLens detector, a working distance of 3.2 mm and an acceleration voltage of 5 kV. The samples were placed on carbon adhesive tape mounted on an aluminium SEM stub. Before imaging, the samples were sputter coated (10 nm) using a Pd/Pt metal target (Cressington 108 auto), provided with a thickness controller. The coating was applied to minimize charging on the surface of the sample due to the back scattering of the electron beam when hitting non-electrical conductive materials and under a weak argon atmosphere.

TEM imaging of samples was performed using a FEI Talos F200X microscope. BNNS were first sonicated for 5 min in chloroform. Successive drops of the dispersion were placed onto a lacy carbon coated 200 mesh copper grid (Agar scientific) and left at room temperature to allow solvent evaporation.

The crystalline structure of BNNS was analysed by Wide-angle X-ray diffraction (WAXD), using a PANalytical Empyrean X-ray diffractometer. The instrument was equipped

View Article Online
DOI: 10.1039/C8NR06429F

with a Co ($K_{\alpha 1}$ (λ) = 1.789 Å) source, a PIXcel^{3D} detector, a tube voltage of 45 kV and current of 40 amps. The tests were set in reflectance mode with a stage speed of 1 rps.

A Renishaw in Via Reflex confocal Raman microscope (Gonzo) equipped with a 532 nm solid state laser and x5, x20, x50 objectives was used to perform Raman measurements. The instrument was equipped with a Renishaw CCD detector (Visible – NIR) and a 10 mW laser, which was spot focused on the sample with an exposure time of 2 min and 5 collections.

XPS measurements were performed using a Kratos Axis Ultra delay-line-detector XPS. The instrument was equipped with a magnetic immersion lens and charge neutralisation system with spherical mirror and concentric hemispherical analysers. Measurements were analysed using CasaXPS analysis software.

Sessile tests were performed using a Dyne Testing-ThetaLite instrument, provided with a camera and a light source for optical measurements. The sample in pellet form was placed onto the stage and a drop of distilled water (~6 µL) placed onto the sample surface by using a manual dispenser. Five measurements were carried out at five different points on the pellet. The images were recorded at room temperature over a time range of 10 s and at 10% FPS. The software method set for the contact angle elaboration was based on Young-Laplace.

Nitrogen adsorption/desorption isotherms were measured at -196 °C on a Micromeritics ASAP2020 system. The samples were out-gassed at 300 °C for 4 h prior to the sorption measurements. The Brunauer-Emmett-Teller (BET) equation was used to calculate the specific surface area in the range of relative pressure between 0.05 and 0.25.

A Mettler Toledo TGA1-STARe system was used to assess the thermal stability of BNNS under oxidative conditions. The samples was placed in to 70 µL alumina pans and heated from room temperature to 800 °C at a constant heating rate of 10 K/ min. The resulting TGA and DTGA curves were plotted in a x-y graph, where the y-axis was defined

View Article Online
DOI: 10.1039/C8NR06429F

as % weight loss/100 as a function of temperature (°C), in order to set a compatible scale for both TGA and DTGA values.

3. Results and Discussion

Figure 1 (a-d) shows the SEM images of BNNS produced, at different magnifications.

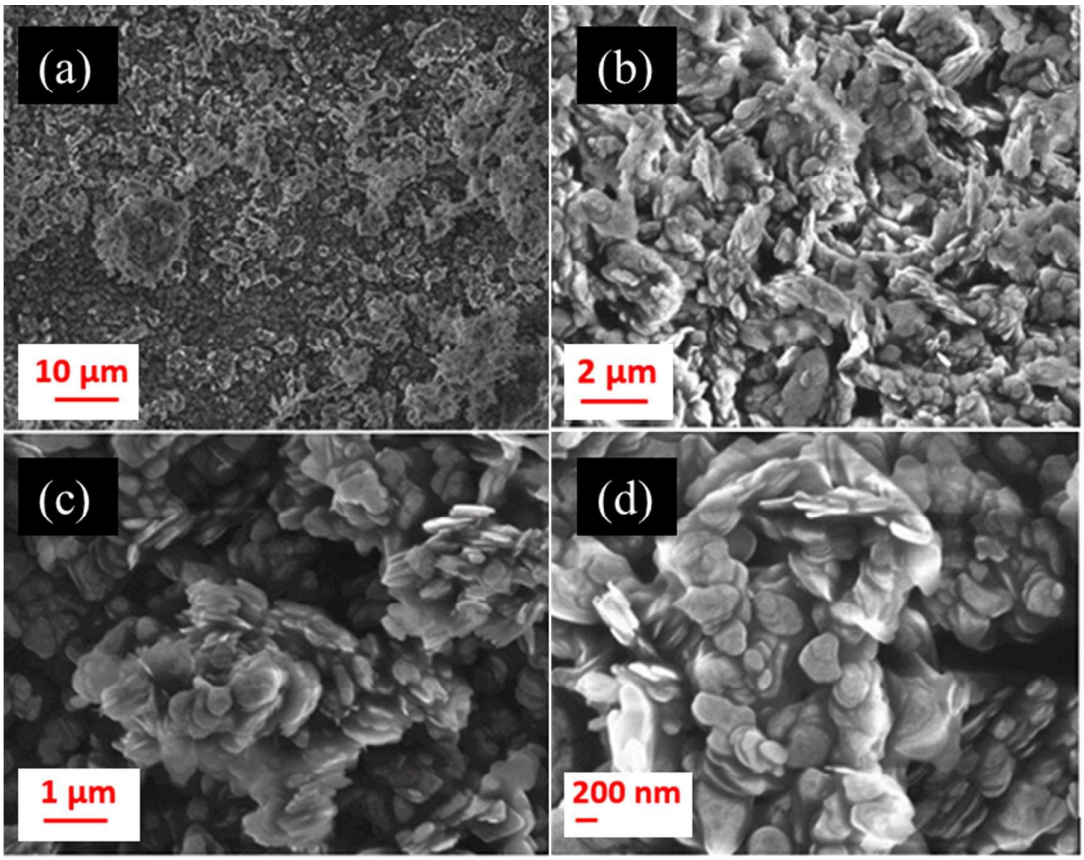

Figure 1. Scanning Electron Microsacopy (SEM) images of BNNS at different magnifications.

BNNS agglomerates on the micrometre scale are arranged in a layered structure with irregular round shapes, whereas they have lateral dimensions on the nanometre scale. Due to their irregular flake-like structure, it is not possible to estimate the dimensions of a single BNNS platelet because an exact value of the lateral dimensions would not be accurate. The shape and dimensions of BNNS are the result of the exfoliation procedure of the bulk

View Article Online
DOI: 10.1039/C8NR06429F

material where fragmentation occurs. Andrea Liscio *et al.* [32] asserted that there are two main fragmentation processes where the sheets collide, shrink and eventually break down: (i) bulk and (ii) edge fragmentation. In "bulk fragmentation", large platelets are broken into pieces with comparable dimensions and shapes. In "edge fragmentation", small pieces are broken off from the edge of the larger platelets by an erosion process. Since BNNS show round-shaped layers having small platelets, one could speculate that for this BNNS, edge fragmentation was the dominant process resulting in the formation of small and smooth sheets. However, the reason why BNNS is prone to a specific fragmentation process is not yet clear. It may be possible that during bulk fragmentation BNNS breaks easily along the single bond B-N (bond energy = 389 kJ/mol in gaseous phase at 298 K [33]). This results in the formation of a high number of small sheets, which collide with each other and are more likely to erode than break down further.

View Article Online
DOI: 10.1039/C8NR06429F

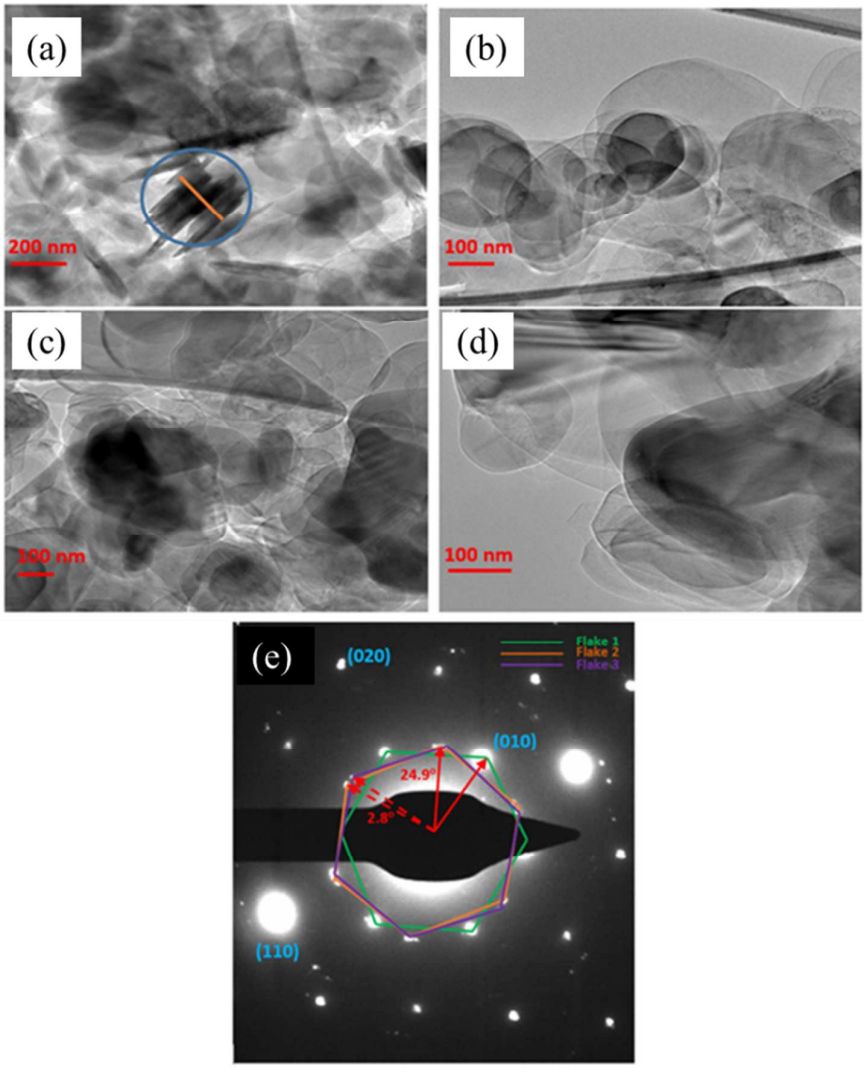

Figure 2. TEM images (a-d) and Selected Area Electron Diffraction (SAED) pattern (e) of BNNS.

Figure 2 (a-e) shows the TEM images of BNNS. Semi-transparent layers are visible suggesting the presence of very thin flakes, which coexist with thick ones as evident from darker regions (a-d). In Figure 2a, BNNS flake is seen along its transversal axis (blue circle) showing a thickness of *ca*. 200 nm (orange line). The Selected Area Electron Diffraction (SAED) pattern in Figure 2e shows the most intense diffracted crystalline planes (010), (110) and (020). The typical hexagonal structure of BNNS is evident from the drawn hexagons, which identify three flakes oriented differently from each other. The most intense flake

View Article Online
DOI: 10.1039/C8NR06429F

(green path) is rotated 24.9° from the second flake (orange path) which in turn is rotated 2.8° from the third flake (purple path). Therefore, the BNNS presents a polycrystalline structure with twisted flakes [34, 35].

The crystalline structure analysis of BNNS and the starting bulk material (h-BN) was performed using X-Ray diffraction (XRD), shown in Figure 3.

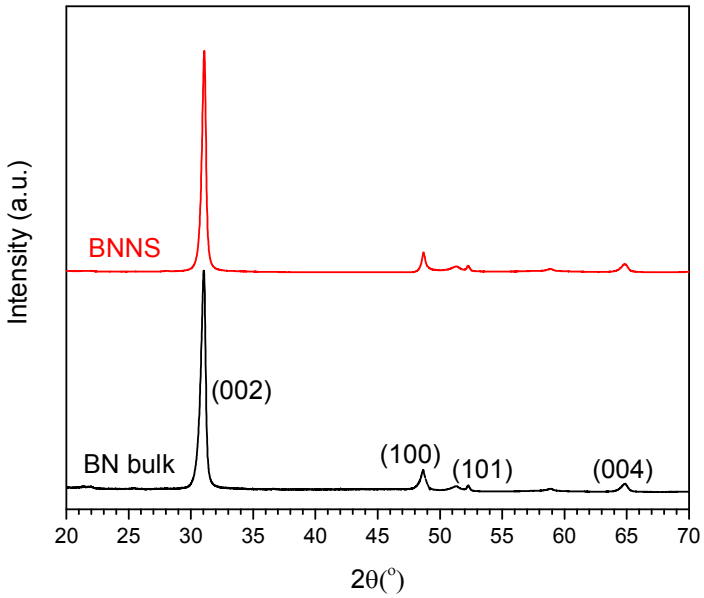

Figure 3. X-Ray Diffraction (XRD) pattern of bulk h-BN and BNNS.

The XRD patterns reveal a highly crystalline structure with the most intense and sharp peak observed at 2θ = 31°, which is due to the crystallographic plane (002) of BN. The weaker peaks in the patterns are due to the crystallographic planes of (100), (101) and (004) at 2θ= 48.5°, 52°, 65° respectively. It should be noted that the peaks are slightly shifted compared to earlier reports, as the diffractometer used in this work has a cobalt X-ray source rather than copper. Therefore, the experimental wavelength is $\lambda_{CoK\alpha1}$= 1.789 Å and not $\lambda_{CuK\alpha1}$= 1.5418 Å [36-38]. By comparing the h-BN bulk and BNNS XRD spectra, it is evident that the peaks remained unchanged in both materials in terms of diffraction angle and shape, suggesting that the high-pressure homogenisation exfoliation process did not damage the

View Article Online
DOI: 10.1039/C8NR06429F

crystalline structure of the pristine material. BNNS retained the high crystalline structure of the bulk BN.

Further analysis of the BNNS spectra, using Bragg's law, allows the calculation of the interlayer distance for BNNS:

$$d_{hkl} = \frac{\lambda}{2sin\theta} \qquad (1)$$

where, d_{hkl} is the interlayer distance in nm corresponding to the crystalline plane (hkl), λ is the X-Ray wavelength source (nm) and θ is the diffraction angle (rad) corresponding to the plane (hkl). By considering the crystalline plane (002) at 2θ = 31°, the interlayer distance is 0.335 nm, in good agreement with values reported previously [36-38].

Using the Scherrer equation, it is possible to calculate the dimension L_{hkl} of the crystallites along the direction perpendicular to the crystalline plane (hkl), in effect the thickness:

$$L_{hkl} = \frac{k\lambda}{\beta_{hkl}cos\theta_{hkl}} \qquad (2)$$

where, k is a constant depending on the modelled shape of the crystallites with values between 0.89-0.94. In this case, a k value of 0.9 was used [36]. β_{hkl} is the FWHM of the peak corresponding to the plane (hkl) and θ is the diffraction angle (rad) of that plane [36]. By applying the Scherrer equation to the crystalline plane (002) at 2θ=31°, the resulting dimension L_{002} (thickness) is found as 2 nm. By considering the calculated interlayer distance (0.335 nm) and the calculated thickness (2 nm) for the plane (002), it is possible to assert that the peak at 2θ=31° is due to the contribution of six crystalline equidistant parallel planes (002).

The XRD results for BNNS are summarised in Table 1.

View Article Online
DOI: 10.1039/C8NR06429F

Table 1. X-ray Diffraction (XRD) results for BNNS.

Crystalline planes/2θ	(002)/31°
	(100)/48.5°
	(101)/52°
	(004)/65°
$d_{(002)}$	0.335 nm
$L_{(002)}$	2 nm
N° crystalline planes (002)	6

It is evident that the diffracted crystal planes registered in XRD are different from the ones identified in SAED. In fact, the main diffracted planes in XRD are (002), (100), (101) and (004) while in SAED they are (010), (110) and (020). This is common when comparing the two diffraction techniques. The electron wavelength in SAED (λ= 0.00251 Å) is much shorter than the wavelength in XRD ($\lambda_{CoK\alpha1}$= 1.789 Å); that is the diffraction angles in SAED are much smaller than in XRD. Therefore, the diffracted rays from crystalline planes at smaller angles recorded in SAED might not be recorded in XRD. Moreover, multiple scattering in SAED is common due to the stronger interaction of matter with electrons than with X-rays which can lead to reflections in SAED, which are not registered in XRD.

Figure 4 shows the Raman spectra of bulk BN and BNNS.

View Article Online
DOI: 10.1039/C8NR06429F

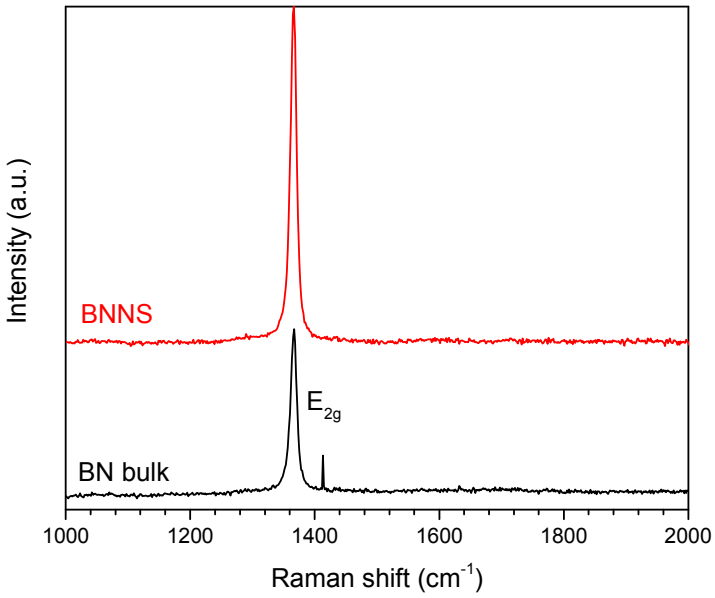

Figure 4. Raman spectra of bulk BN and BNNS.

The peak at 1360 cm^{-1} is the characteristic Raman active vibrational mode (E_{2g}) of the hexagonal BN. In particular, it is due to the in plane vibration of the sp^2 hybridized B-N=B bond. This peak is intense and narrow in BNNS, suggesting a low concentration of defect structures [39, 40]. Li Song *et al.* [39] proposed that the FWHM of the E_{2g} peak decreases from 15.5 cm^{-1} to 11.7 cm^{-1} as the bulk material is compared to a thin layered material. We found that, the FWHM of the E_{2g} peak shifted from 15 cm^{-1} to 12.5 cm^{-1} as BN-bulk transforms into BNNS, suggesting that the high-pressure homogenisation process was effective in exfoliating the bulk material to thinner flakes of BNNS. (The small sharp peak at 1420 cm^{-1} is an artefact of the measurement and not related to BNNS).

The chemical composition of the BNNS surface was studied using X-ray photoelectron spectroscopy (XPS) and the spectra recorded were analysed by CasaXPS software. The results are shown in Figure 5 and the main features are summarised in Table 2.

View Article Online
DOI: 10.1039/C8NR06429F

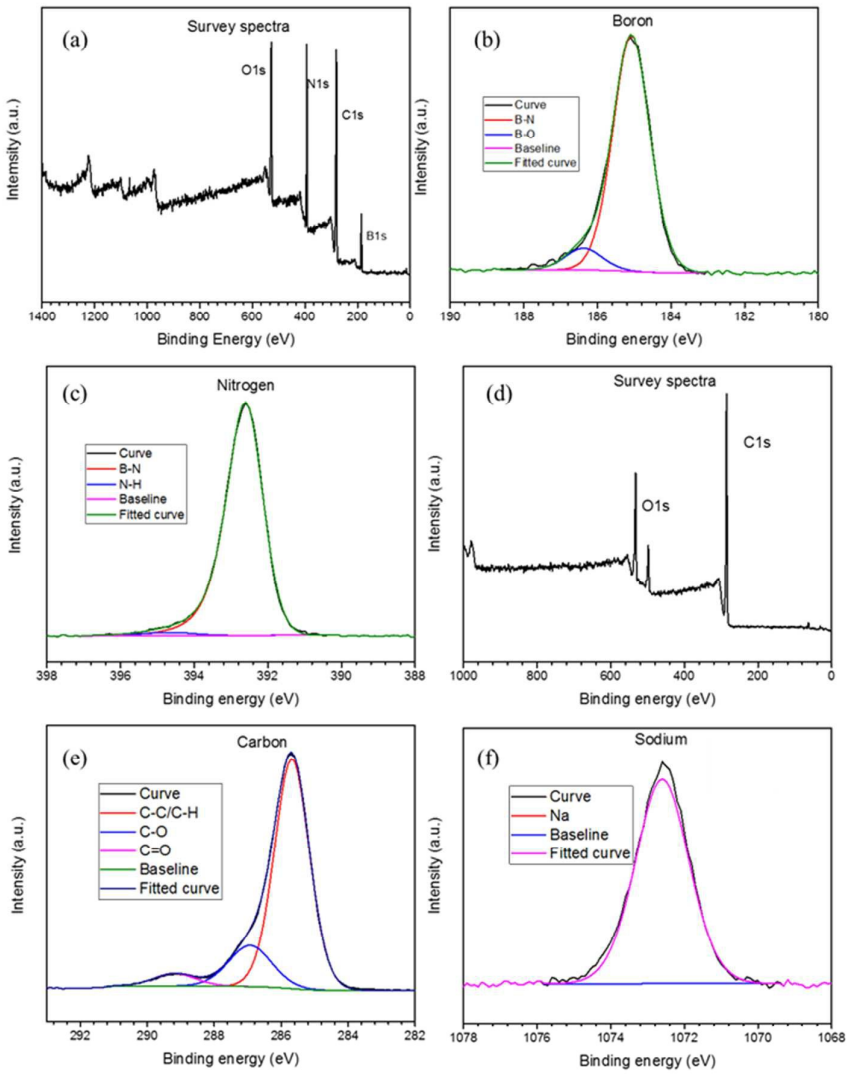

BNNS	
Name	*Atoms (%)*
B1s	20.32
N1s	18.39
C1s	48.04
O1s	13.21
Na1s	0.05
Surfactant	
Name	*Atoms (%)*
C1s	78.37
O1s	17.05
Na1s	4.58

(g)

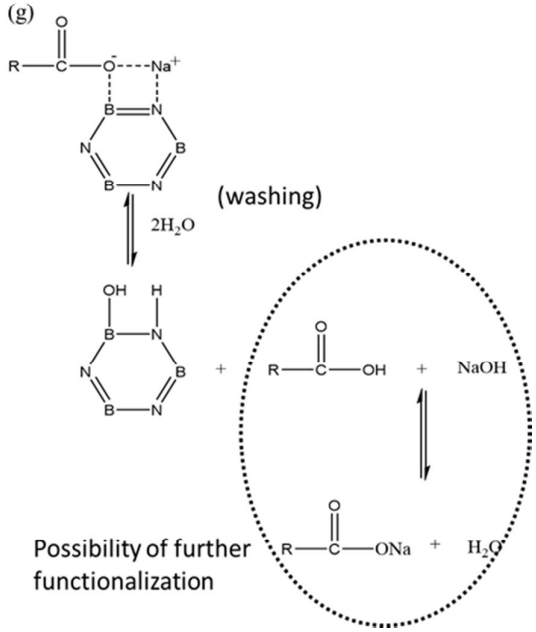

View Article Online
DOI: 10.1039/C8NR06429F

Figure 5: X-Ray photoelectron spectroscopy (XPS) results of BNNS (a-c); survey spectra (a), boron (b) and nitrogen (c) peaks. XPS results of the sodium cholate surfactant used during BNNS preparation processing; survey spectra (d), carbon (e) and sodium (f) peaks. Possible interaction mechanism between BNNS and the surfactant (g).

Table 2. Summary of XPS peaks identified for BNNS.

Material	Detected atoms	Main peaks	Lorentzian/Gaussian components
BNNS	B1s	190 eV	B*-N (190 eV)
			B*-OH (192.5 eV)
	N1s	397.5 eV	B-N* (397.5 eV)
			N*-H (400 eV)
	C1s	284.5 eV	-
	O1s	532.5 eV	-
	Na1s	1071 eV	-

The XPS survey spectra of BNNS (a) identifies B1s, N1s, O1s, C1s and Na1s peaks at 190 eV, 397.5 eV, 532.5 eV, 284.5 eV and 1071 eV, respectively [36, 41]. The ratio of B:N is 1:1 suggesting that the exfoliation process did not damage the hexagonal structure of the bulk BN material. The presence of oxygen, carbon and sodium are impurities from the atmosphere and the surfactant (sodium cholate) used in this instance during the exfoliation process. The higher resolution core-level photoemission spectra of B1s and N1s (b, c) show asymmetric and broad peaks, suggesting that boron and nitrogen atoms in BNNS are involved in a more complex bonding scheme than simple B-N=B bonding. In fact, both B1s and N1s spectra were fitted by two curves, a combination of Lorentzian/Gaussian profiles. The main curve for

View Article Online
DOI: 10.1039/C8NR06429F

B1s at 190 eV is due to the B-N bond, while the second curve at 192.5 eV is due to the B-OH bond [36, 41]. N1s spectra show the main curve at 397.5 eV is due to B-N bonding, while the second curve at 400 eV is due to N-H bonding [36, 41]. The B-OH and N-H bonds can be associated with interactions between BNNS and the surfactant used during the exfoliation process. This observation was also supported by the presence of sodium in the survey spectra of BNNS and by the presence of carbon with higher concentration than it would be expected as an impurity from the atmosphere. The spectra of the pure surfactant (d-f) and the possible interaction mechanism with BNNS are shown in Figure 5g.

The presence of B-OH and N-H groups on the BNNS surface as detected by XPS reveals the hydrophilic nature of BNNS. This observation was confirmed by performing sessile tests, with distilled water as the reference liquid. The results, registered over a time span of 10 s, shows the change of the contact angle from 60°±3° at 0 s to 40°±2° at 10 s, confirming the hydrophilic behaviour of the BNNS surface. Figure 6 shows the contact angle images at 0 s and 10 s for BNNS:

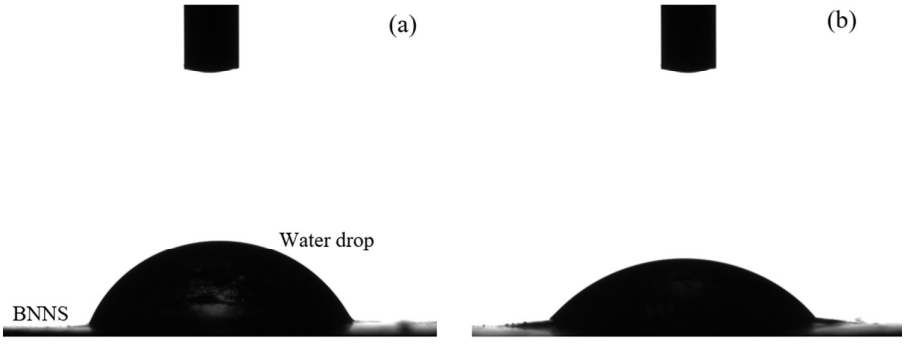

Figure 6: Contact angle images of BNNS with water as the reference liquid at 0 s (a) and 10 s (b).

View Article Online
DOI: 10.1039/C8NR06429F

Further surface characterization of BNNS was carried out by the nitrogen physisorption at -196 °C. The adsorption and desorption isotherms are shown in Figure 7.

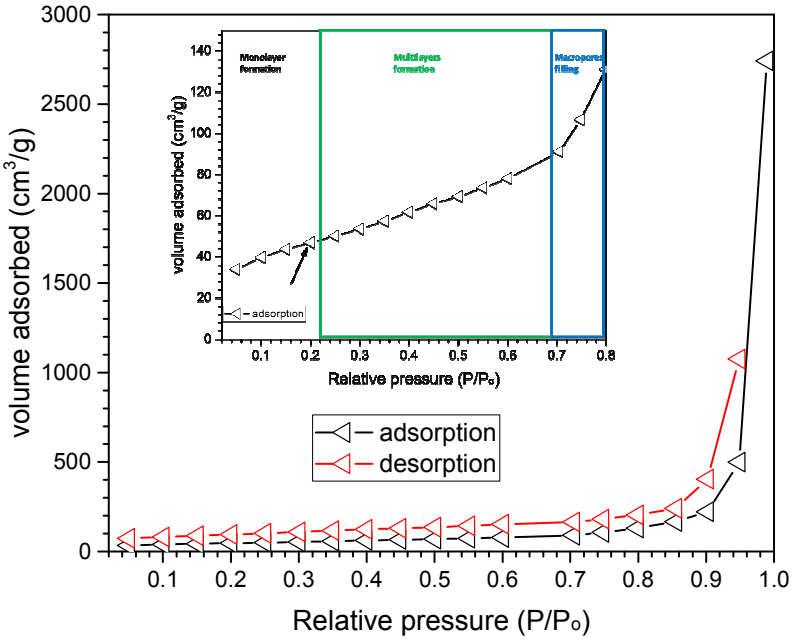

Figure 7. Nitrogen adsorption (black curve) and desorption (red curve) isotherms of BNNS. Inset shows the adsorption isotherm only.

The N_2 adsorption/desorption isotherms are typical of a macroporous material identified as a type II isotherm according to the IUPAC classification [42] accompanied by a hysteresis. At a relative pressure of *ca.* 0.25, a complete nitrogen monolayer is formed on the BNNS surface (Figure 7 inset, black arrow), followed by the formation of nitrogen multilayers as evident from the quasi-linear region at relative pressure of *ca* 0.25-0.7. At relative pressures above 0.7, the curve rapidly increases due to the filling of macro-pores and no condensation occurs. This behaviour is typical of adsorbents having a wide pore size distribution and can be explained by Kelvin's law,

$$ln\frac{P}{P_o} = \frac{2\gamma V_m}{rRT} \quad (3)$$

View Article Online
DOI: 10.1039/C8NR06429F

where, P/P_o is the relative pressure with P= pressure of adsorbate and P_o= saturated pressure of adsorbate, γ is the surface tension of the liquid (condensed)/vapour, V_m is the molar volume of adsorbate, r is the radius of curvature of liquid meniscus, R is the universal gas constant and T is the absolute temperature. It should be emphasised that r is not the radius of the pores, which is instead given by summing r and the thickness of the adsorbed molecules.

For a defined physical system, the unique variables in Kelvin's equation are P/P_o and r. In the first phase of adsorption, the meniscus is flat ($r=\infty$) and no condensation occurs ($P/P_o=1$, $\ln(P/P_o)=0$). With the increase of the number of adsorbed layers, the meniscus starts to approach a concave profile and eventually it is concave upon condensation of the gas. However, in a macro-porous material such as the BNNS studied, condensation does not occur because the pores are not small enough to create a strict confined place where the gas molecules are forced to diffuse. In such conditions, they are not subject to attractive Van Der Waals forces, which ultimately causes the transition from gas to liquid. That is, the meniscus does not reach a concave profile and no condensation can be detected. The change of the meniscus profile during adsorption is represented in Figure 8.

View Article Online
DOI: 10.1039/C8NR06429F

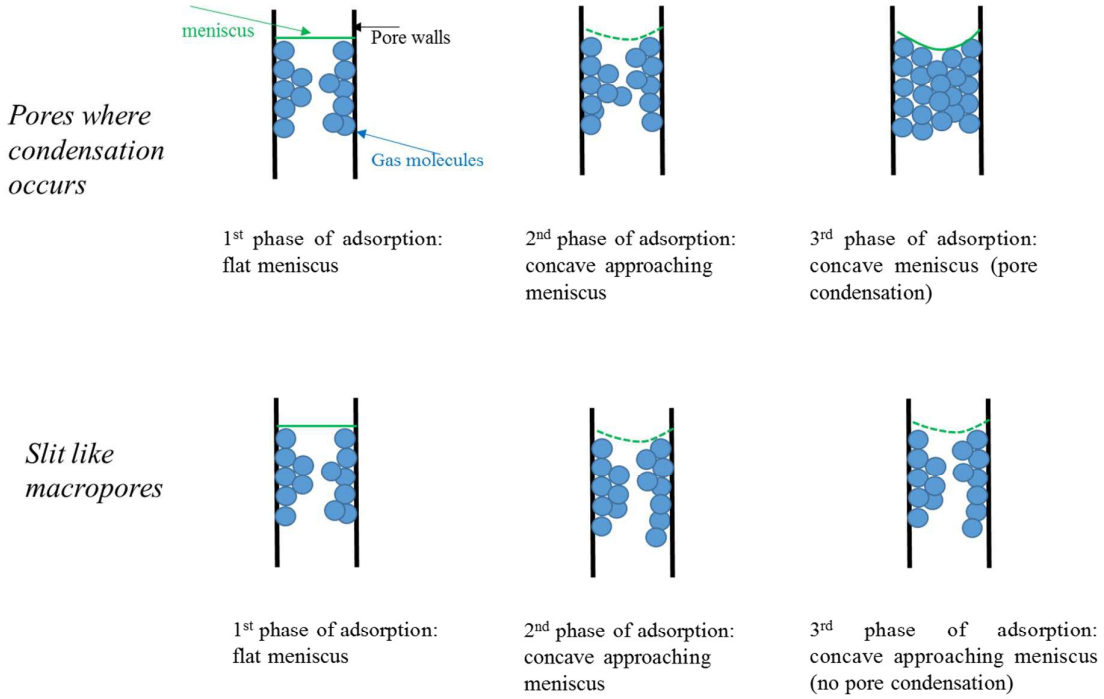

Figure 8. Schematic showing meniscus formation from flat to concave in the case of pore condensation and from flat to quasi-concave in slit like macro-pores where no condensation occurs. (The meniscus is represented from the first layer of the adsorbed gas to make the concept easy to comprehend at first glance. However, the real meniscus takes into account only the condensed molecules of the adsorbate. The adsorbed layers constitute the thickness of adsorbed gas on the pore walls, thereby contributing to the estimation of pore size).

The insert in Figure 7 is a magnification of the adsorption isotherm to highlight the monolayer formation end-point (black arrow), the quasi-linear region and the macro-pore filled region. By applying the Brunauer-Emmet-Teller (BET) equation in the range of relative pressure 0.05-0.25, the specific surface area of BNNS was calculated to be *ca.* 170 m^2/g.

The reported desorption curve shows hysteresis, identified as type H3 according to the IUPAC classification [42]. It is due to the presence of slit-like pores formed by the agglomeration of sheets-like particles having non-uniform shape and/or size, in agreement with the SEM and TEM images, see Figures 1 and 2. The hysteresis is due to a different

View Article Online
DOI: 10.1039/C8NR06429F

behaviour of the adsorbate during adsorption and desorption. While the meniscus is flat during adsorption, during desorption the meniscus is either concave (condensation) or quasi-concave (pores are being filled but no condensation occurs), as depicted in Figure 8. The difference in the profile of the meniscus between adsorption and desorption implies a different thermodynamic system and behaviour of the adsorbate in terms of relative pressure at which a specific volume of adsorbate is first adsorbed and then desorbed. Furthermore, the low pressure closure of nitrogen hysteresis takes place at a relative pressure of 0.42, due to the tensile strength effect of liquid (condensed) nitrogen. The tensile strength of a liquid is the maximum strength that a liquid can withstand before passing to gas phase. During desorption, the tension of the condensed nitrogen increases as P/P_o decreases, reaching the maximum value possible (tensile strength) at relative pressure of 0.42, which is the critical condition for nitrogen to be still liquid. Below this point, no condensed nitrogen can exist, therefore in the case of condensation the hysteresis must close at $P/P_o=0.42$. However, in BNNS nitrogen does not condense at all, thus the hysteresis loop closes at relative pressure far below 0.42, due to the gas still trapped in the structure, which keeps desorbing. The low pressure hysteresis may be caused by the geometry of the pores, a change of pore volume, swelling of non-rigid pores, irreversible uptake of nitrogen in the pores and chemisorption. Ultimately, it is not possible to accurately study the pore size distribution of BNNS with the isothermal adsorption/desorption technique [42, 43].

The thermal stability of BNNS was evaluated from thermogravimetric analysis (TGA), as shown in Figure 9.

View Article Online
DOI: 10.1039/C8NR06429F

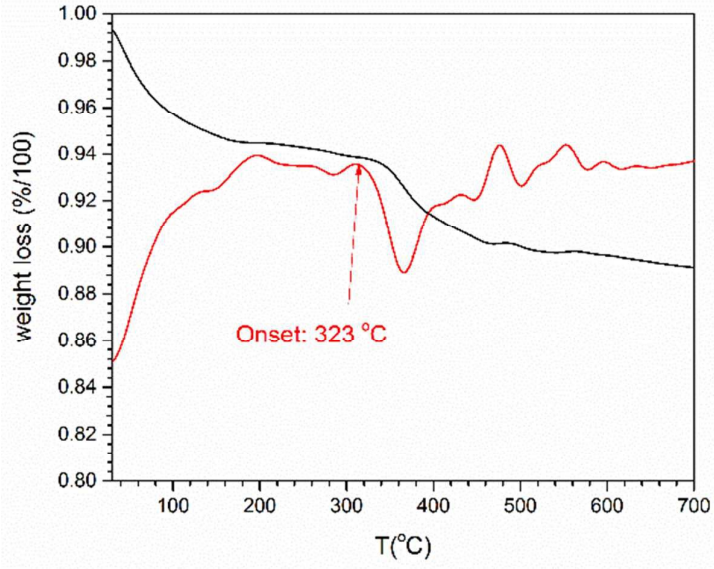

Figure 9: TGA and DTG curves for BNNS under oxidative conditions from 25 ^{o}C to 700 ^{o}C at 10 K/min. Weight loss (%/100) (black) and the first derivative (DTGA) (red) as a function of temperature T (^{o}C).

BNNS are thermally stable under oxidative conditions and start to degrade at around 323 °C. The weight loss registered below the degradation point is due to the residual water used during the exfoliation process and corresponds to 6wt%. Due to the weight loss of residual water in the range of 5-10wt%, the degradation onset has been identified at the knee of the inflection point in the TGA curve (black), which corresponds to the knee of the main minimum peak in the DTGA curve (red). Degradation stopped at around 500 °C reaching a plateau with a residue of about 88wt %.

4. Conclusions

High-pressure homogenisation is an effective process for the exfoliation of bulk h-BN to form BNNS.

View Article Online
DOI: 10.1039/C8NR06429F

Technique	Results
SEM	μm thick flakes nm length sheets
TEM **SAED**	Thin and thick flakes coexistence Polycrystalline structure
XRD	$2\theta=31° \rightarrow (002)$ $d_{002} = 0.335$ nm $L_{002} = 2$ nm
Raman	1360 $cm^{-1} \rightarrow E_{2g}$ Sharp peak → low defects concentration FWHM = 12.5 cm^{-1} → exfoliated structure
XPS	B-OH and N-H groups formation onto BNNS surface; presence of surfactant residue
Sessile test	Contact angle: 60° ±3° (0 s) 40°±2° (10 s)
N_2 ads/des Isotherms **BET**	Macro-porous material; slit-like pores Surface area: 170 m^2/g
TGA	Degradation onset (under oxidative

Table 3. Properties of BNNS.

View Article Online
DOI: 10.1039/C8NR06429F

conditions): 323°C

SEM analysis of BNNS revealed a flake structure with round-shaped platelets on the nanometre length scales. In TEM images, few layered nanosheets and thicker agglomerates were observed. SAED showed the typical hexagonal structures of BNNS with polycrystalline flakes rotated from each other with orientation angles between *ca* 3° and 30°. XRD patterns revealed a highly crystalline structure with the most intense peak at 2θ = 31° due to the crystallographic plane (002) of BNNS. By applying Bragg's law and the Scherrer equation, the calculated interlayer distance and dimensions (L_{002} thickness) are 0.335 nm and *ca* 2 nm respectively. That is, the peak at 2θ = 31° is associated with a contribution from six crystalline equidistant parallel planes (002). Raman spectra revealed the main peak at 1360 cm^{-1} which is due to the active vibrational mode E_{2g}; typical of the hexagonal structure of boron nitride. The peak is intense and narrow, suggesting that the BNNS have a low defect density and the FWHM is 12.5 cm^{-1}, indicating an exfoliated structure. XPS analysis revealed the presence of impurities on BNNS surface, originating from the surfactant used during the exfoliation process. This lead to a slight functionalization of the BNNS surface as evident from the combined Lorentzian/Gaussian curves of B-OH and N-H bonds at 192.5 eV and 400 eV respectively. Furthermore, the presence of B-OH and N-H groups suggested a hydrophilic BNNS surface, confirmed from sessile tests where the contact angle of BNNS was 60°±3° (0 s) and 40°±2° (10 s). Nitrogen adsorption/desorption isotherms revealed BNNS as a macro-porous material with slit-like pores formed by the agglomeration of sheet-like particles having non-uniform shape and size and a BET surface area of 170 m^2/g. The TGA of BNNS showed high resistance to thermal degradation under oxidative conditions (T_{onset}=323 °C).

View Article Online
DOI: 10.1039/C8NR06429F

Acknowledgments

VG thanks the EPSRC and Thomas Swan & Co Ltd for funding an EngD. The authors thank Dr Jaipal Gupta, Dr Marc Walker, Dr Samuel Marks, Miss Syeda S. Abbas and Mr Martin Worrall for technical assistance.

References

[1] Meng WJ, Huang Y, Fu YQ, Wang ZF, Zhi CY 2014 *J. Mater. Chem. C* **2** 10049-61.

[2] Jo I, Pettes MT, Kim J, Watanabe K, Taniguchi T, Yao Z, Shi L 2013 *Nano Lett.* **13** 550-4.

[3] Kiran MSRN, Raidongia K, Ramamurty U, Rao CNR 2011 *Scripta Mater.* **64** 592-5.

[4] Kim K, Kim J 2014 *Ceram. Int.* **40** 5181-9.

[5] Novoselov KS, Geim AK, Morozov SV, Jiang D, Zhang Y, Dubonos SV, Grigorieva IV, Firsov AA 2004 *Science* **306** 666-9.

[6] Li LH, Chen Y, Behan G, Zhang HZ, Petravic M, Glushenkov AM 2011 *J. Mater. Chem.* **21** 11862-6.

[7] Pakdel A, Zhi CY, Bando Y, Golberg D 2012 *Mater. Today* **15** 256-65.

[8] Pakdel A, Bando Y, Golberg D 2014 *Chem. Soc. Rev.* **43** 934-59.

[9] Han WQ, Wu LJ, Zhu YM, Watanabe K, Taniguchi T 2008 *Appl. Phys. Lett.* **93** 3.

[10] Nag A, Raidongia K, Hembram K, Datta R, Waghmare UV, Rao CNR 2010 *ACS Nano* **4** 1539-44.

[11] Pierson HO 1975 *J. Compos. Mater.* **9** 228-40.

[12] Adams AC 1981 *J. Electrochem. Soc.* **128** 1378-9.

[13] Muller F, Stowe K, Sachdev H 2005 *Chem. Mater.* **17** 3464-7.

[14] Archer NJ 1979 *Phys. Techn.* **10** 152-61.

[15] Jin C, Lin F, Suenaga K, Iijima S 2009 *Phys. Rev. Lett.* **102**.

[16] Meyer JC, Chuvilin A, Algara-Siller G, Biskupek J, Kaiser U 2009 *Nano Lett.* **9** 2683-9.

View Article Online
DOI: 10.1039/C8NR06429F

[17] Zhang X, Shen L, Wu H, Guo S 2013 *Compos. Sci. Technol.* **89** 24-8.

[18] Zhou W, Qi S, Li H, Shao S 2007 *Thermochim. Acta* **452** 36-42.

[19] Mosanenzadeh SG, Naguib HE 2016 *Compos. Part B-Eng.* **85** 24-30.

[20] Hou J, Li GH, Yang N, Qin LL, Grami ME, Zhang QX, Wang NY, Qu XW 2014 *Rsc. Adv.* **4** 44282-90.

[21] Jin W, Zhang W, Gao Y, Liang G, Gu A, Yuan L 2013 *Appl. Surf. Sci.* **270** 561-71.

[22] Muratov DS, Kuznetsov DV, Il'inykh IA, Burmistrov IN, Mazov IN 2015 *Compos. Sci. Technol.* **111** 40-3.

[23] Kim K, Kim M, Hwang Y, Kim J 2014 *Ceram. Int.* **40** 2047-56.

[24] Yu J, Huang X, Wu C, Wu X, Wang G, Jiang P 2012 *Polymer* **53** 471-80.

[25] Naskar AK, Keum JK, Boeman RG 2016 *Nat. Nanotechnol.* **11** 1026-30.

[26] Tanimoto M, Yamagata T, Miyata K, Ando S 2013 *ACS Appl. Mater. Interfaces* **5** 4374-82.

[27] Yuan C, Duan B, Li L, Xie B, Huang MY, Luo XB 2015 *ACS Appl. Mater. Interfaces* **7** 13000-6.

[28] Yuan C, Xie B, Huang M, Wu R, Luo X 2016 *Int. J. Heat Mass Transfer* **94** 20-8.

[29] Kim K, Kim J 2016 *Int. J. Therm. Sci.* **100** 29-36.

[30] Shang JQ, Xue F, Fan CJ, Ding EY 2016 *Mater. Lett.* **181** 144-7.

[31] Ladislaus Paul, Glasgow Lee, McHale Ronan 2017;WO 2017/064496 A1:1-11.

[32] Liscio A, Kouroupis-Agalou K, Betriu XD, Kovtun A, Treossi E, Pugno NM, De Luca G, Giorgini L, Palermo V 2017 *2D Mater.* **4**.

[33] Dean JA. *Lange's Handbook of Chemistry*. fourteeth ed. New York: McGraw-Hill, Inc. 1999.

[34] Lee D, Song SH, Hwang J, Jin SH, Park KH, Kim BH, Hong SH, Jeon S 2013 *Small* **9** 2602-10.

View Article Online
DOI: 10.1039/C8NR06429F

[35] Zhi CY, Bando Y, Tang CC, Kuwahara H, Golberg D 2009 *Adv. Mater.* **21** 2889-+.

[36] Nazarov AS, Demin VN, Grayfer ED, Bulavchenko AI, Arymbaeva AT, Shin HJ, Choi JY, Fedorov VE 2012 *Chem. Asian J.* **7** 554-60.

[37] Kostoglou N, Polychronopoulou K, Rebholz C 2015 *Vacuum* **112** 42-5.

[38] Kostoglou N*, et al.* 2016 *Mater. Des.* **110** 540-8.

[39] Sajjad M, Morell G, Feng P 2013 *ACS Appl. Mater. Interfaces* **5** 5051-6.

[40] Chubarov M, Pedersen H, Hogberg H, Filippov S, Engelbrecht JAA, O'Connel J, Henry A 2014 *Physica B Condens. Matter* **439** 29-34.

[41] Song L*, et al.* 2010 *Nano Lett.* **10** 3209-15.

[42] Leofanti G, Padovan M, Tozzola G, Venturelli B 1998 *Catal. Today* **41** 207-19.

[43] Sing KSW, Everett DH, Haul RAW, Moscou L, Pierotti RA, Rouquerol J, Siemieniewska T 1985 *Pure Appl. Chem.* **57** 603-19.

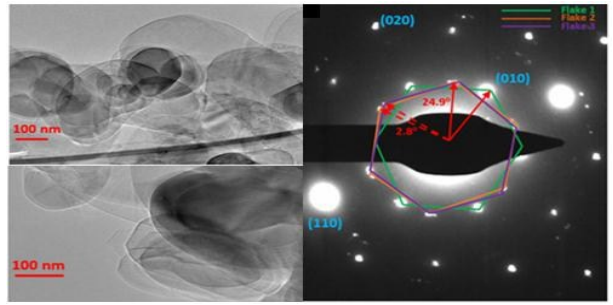

Polycrystalline boron nitride nano-sheets (BNNS) were prepared via a scalable high-pressure homogenization process.